This is the published version of a paper published in *Optics Express*.

Access to the published version may require subscription.

N.B. When citing this work, cite the original published paper.

Time-resolved continuous-filtering Vernier spectroscopy of H_2O and OH radical in a flame

CHUANG LU,[1,3] FRANCISCO SENNA VIEIRA,[1,3] FLORIAN M. SCHMIDT,[2] AND ALEKSANDRA FOLTYNOWICZ[1,*]

[1]*Department of Physics, Umeå University, 901 87 Umeå, Sweden*
[2]*Department of Applied Physics and Electronics, Umeå University, 901 87 Umeå, Sweden*
[3]*These authors contributed equally to this work*
*aleksandra.foltynowicz@umu.se

Abstract: We use broadband near-infrared continuous-filtering Vernier spectroscopy (CF-VS) for time-resolved detection of H_2O and OH radical in a premixed CH_4/air flat flame. The CF-VS spectrometer is based on a femtosecond Er:fiber laser, an external cavity that contains the flame, and a detection system comprising a rotating diffraction grating and photodetectors. Spectra of H_2O and OH radical around 1570 nm are continuously recorded with 6.6 GHz spectral resolution, 4.0×10^{-7} cm^{-1} absorption sensitivity, and 25 ms time resolution, while the fuel-air equivalence ratio is periodically modulated with a square wave. The concentrations of the two analytes are retrieved with percent level precision by a fit of a Vernier model to each spectrum spanning 13 nm. The temporal profiles of both concentrations in each modulation cycle are repeatable and the steady-state concentration levels are in good agreement with predictions based on one-dimensional simulations of a static flat flame. The robust CF-VS spectrometer opens up for quantitative monitoring of multiple products of time-varying combustion processes with relatively simple data acquisition procedures.

1. Introduction

Fast and simultaneous detection of multiple species in combustion is essential for a deeper understanding of chemical reaction dynamics, as well as for obtaining invaluable information and feedback for the design of combustion systems with improved fuel efficiency or decreased pollutant emissions [1,2]. Laser spectroscopic techniques are widely used for combustion diagnostics not only because of their non-intrusiveness but also their high temporal and spatial resolution [3,4]. Among these techniques [5–8] laser absorption spectroscopy is one of the most quantitative methods for selective sensing of gas temperature and composition [9,10]. However, the detection bandwidth of absorption techniques based on continuous wave lasers such as wavelength modulation spectroscopy (WMS) [11,12] and cavity ring-down spectroscopy [13–16] is usually limited to 1–2 cm^{-1} [17,18]. Much larger detection bandwidth is provided by techniques based on broadband sources such as optical frequency combs [19–21], supercontinuum sources [22,23] and Fourier-domain mode-locked lasers [24]. Spectrometers employing these sources have been used to determine water concentration and/or temperature in combustion environments with time resolution of the order of hundreds of microseconds or milliseconds [21,23–25]. However, most of these measurements were done in a single-pass configuration through the sample, limiting the interaction length to a few cm, and thus impairing the absorption sensitivity. So far, time-resolved measurements of species concentrations in dynamically changing combustion environments have not been realized using a broadband cavity-enhanced system. Such system would open up for sensitive multispecies detection in applications where single pass through the combustion process does not provide sufficient sensitivity because of the low analyte abundance or weak line strengths.

Here, we use continuous-filtering Vernier spectroscopy (CF-VS) to detect broadband spectra of H_2O and OH radical in a premixed CH_4/air flame and track the concentrations of these two analytes with time resolution of 25 ms. H_2O and OH are ubiquitous in combustion reactions and therefore of general interest for combustion diagnostics [26–28]. The principle of CF-VS is the generation of tunable frequency filters for the comb using an external cavity [29,30], which also acts as a sample cell. The cavity length is tuned to introduce a small mismatch between its free spectral range (FSR) and the comb repetition rate (f_{rep}). As a result, the cavity resonances form a series of frequency filters that transmit groups of comb lines through the cavity, called Vernier orders (VO). The width of the VO determines the spectral resolution of the system as well as the power transmitted through the cavity. The VOs are continuously swept across the entire bandwidth of the comb by scanning either the cavity FSR or the comb f_{rep}. A diffraction grating positioned after the cavity separates the consecutive VOs and its rotation is synchronized with the spectral scan of the selected VO, keeping the beam spatially fixed on a detector. The entire spectrum in cavity transmission, with bandwidth limited by the comb source, is recorded using a single detector positioned after the grating. The frequency axis of the spectrum is calibrated using either the position information of the grating or spectral fringes introduced by a known etalon element. The acquisition time of a single spectrum is usually of the order of few tens of ms [29–32], limited by the scanning speed of the grating and/or the ring-down time of the cavity, as the scan needs to be adiabatic to avoid distortion in cavity mode profiles [29].

In order to demonstrate the potential of CF-VS for detection of time-dependent concentration profiles in a combustion environment, we record continuously spectra of OH radical and H_2O while the fuel-air equivalence ratio is modulated with a low frequency square wave. To verify the accuracy of the results, the retrieved concentrations of both analytes in the steady-state regions of each modulation cycle are compared to simulated values of a static flame model.

2. Experimental setup and procedures

2.1. Continuous-filtering Vernier spectrometer

The CF-VS setup is depicted in Fig. 1. The spectrometer is based on a mode-locked Er:fiber laser with a repetition rate (f_{rep}) of 250 MHz and a spectral coverage of 1.51–1.58 μm. The oscillator output beam with an optical power of ~20 mW is guided to free space through a polarization maintaining fiber (PMF). The beam is then mode matched using two lenses to an open-air cavity with a length of 60 cm. The beam waist size is around 0.7 mm in the center of the cavity. The cavity finesse was determined by measuring the cavity ring-down times at several wavelengths within the comb bandwidth using a monochromator and an acousto-optic modulator, and was found to vary between 730 to 760. A third-order polynomial fit to these values was later used as an input parameter in the model of the spectra. The cavity length is tuned by ΔL to set the desired VO and spectral resolution by translating a stage (TS) on which one of the cavity mirrors is mounted. A flat flame burner (see section 2.2) positioned in the middle of the cavity is mounted on a vertical translation stage to tune the height of the beam above the burner (HAB). Two mass flow controllers (MFC) set a constant equivalence ratio (ϕ) of air and CH_4 that are premixed and then sent to the burner. Whenever modulation of ϕ is desired, a square wave generated by a function generator (FG 1) drives a solenoid valve (S) in series with a third mass flow controller (MFC 3) that supplies additional air.

The beam transmitted through the cavity is guided by another PMF to a diffraction grating (DG, 600 grooves/mm) mounted on a galvo scanner (GS). Half- and quarter-wave plates are placed before and after the PMF to mitigate spectral etalon fringes, as well as to optimize the diffraction efficiency of the grating. The grating disperses consecutive VOs, and the selected VO is spatially filtered with an iris. After the iris, the beam travels through a 50/50 beam splitter (BS1), from which the reflected arm is incident onto a quadrant detector (QD). The QD outputs a voltage signal proportional to the difference between the intensities incident on the left (D1 + D2)
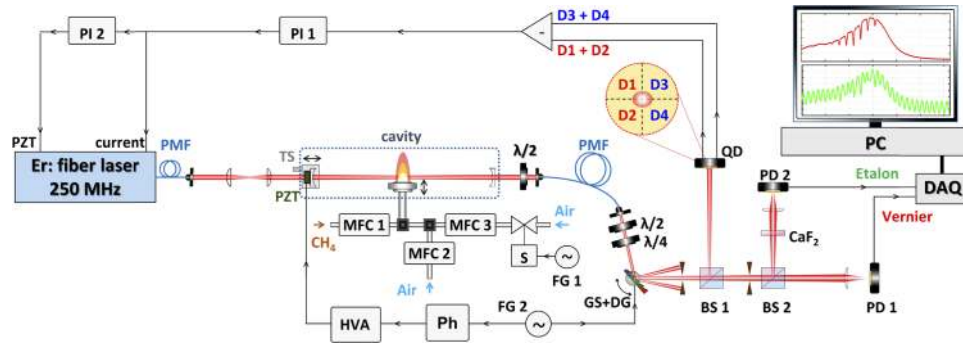
Fig. 1. Experimental setup. PI 1 and 2: proportional integral controllers; PMF: polarization maintaining fiber; PZT: piezo-electric transducer; TS: translation stage; MFC 1-3: mass flow controllers; S: solenoid valve; HVA: high voltage amplifier; Ph: phase shifter; $\lambda/2$ and $\lambda/4$: half- and quarter-wave plates; FG 1 and 2: function generators; GS: galvo scanner; DG: diffraction grating; BS 1 and 2: non-polarizing beam splitters; QD: quadrant detector; D1-4: photo diode elements of the quadrant detector; PD 1 and 2: InGaAs photodiodes for acquisition of Vernier and etalon spectra, respectively; DAQ: multichannel data acquisition card.

and right (D3 + D4) pairs of photodiode elements, and therefore measures the horizontal beam displacement from the detector center. A 20-Hz sinusoidal modulation produced by a low-noise function generator (FG 2) drives the GS and a piezoelectric transducer (PZT) mounted on one of the cavity mirrors to dither the cavity length and sweep the selected VO across the laser spectrum. The GS and PZT scans are synchronized by adjusting the phase and gain of the signal sent to the PZT to keep the VO coarsely fixed in space, and thus minimize the output signal of the QD. However, the different nonlinearities in the GS and PZT responses cause a mismatch between the two scans, resulting in small fluctuations of the beam position on the QD. To remove this mismatch, an active stabilization is implemented, making use of the QD output as an error signal. The error signal is fed to a proportional integral controller (PI 1) that actuates on the pump current of the laser, varying f_{rep} of the comb to compensate the high-frequency fluctuations with a bandwidth of 150 kHz. The low-frequency and high-amplitude fluctuations are compensated by feeding the output of PI 1 to a second PI controller (PI 2). The output of PI 2 controls the f_{rep} of the comb via feedback to the PZT (bandwidth of 6 kHz) attached to one of the laser cavity mirrors.

The beam transmitted by the BS 1 is further split into two arms by another beam splitter (BS 2): one beam is focused directly onto an InGaAs detector (PD 1) for acquisition of the Vernier spectrum, and the other one is sent through a low-finesse etalon (4-mm thick CaF_2 window) and incident onto another InGaAs detector (PD 2) for frequency calibration. The outputs of PD 1 and PD 2 are digitized with a multichannel data acquisition card (DAQ) with 500 kHz sampling rate. Each cycle of the 20-Hz modulation comprises two scans of the full Vernier spectrum, yielding an acquisition time of 25 ms for a single spectrum.

2.2. Flat flame burner

The burner with design similar to that described in [33], Hartung et al., operates on a premixed CH_4/air fuel and generates an axisymmetric flat flame. The burner is cooled with a built-in water circulation, and a nitrogen co-flow is supplied at the outer ring of the burner to stabilize the structure of the flame. In the radial direction, a homogenous flame temperature and distribution of combustion products is assumed. Axially, the flame is cone-shaped with a diameter of 3.8 cm (center ring) at the burner surface. The species concentrations along the center axis are calculated

using the Cantera software [34]. The model employs numerical solutions of the 1-D stagnation flow governing equations with GRI3.0 reaction mechanism. For temperature, we use the results of previous WMS measurements in the same flame [35], which agree with Cantera simulations at lower HABs.

2.3. Spectral acquisition procedures

Prior to every measurement series, the perfect-match length (L_{PM}, for which FSR = f_{rep}) of the cavity is found by translating one of the cavity mirrors to maximize the transmitted power through the cavity while the cavity length is dithered. Next, the VO of the spectrometer is chosen as a trade-off between the signal to noise ratio and spectral resolution. The cavity length is tuned by $\Delta L = -30\,\mu m$, corresponding to VO around -40 (calculated as $2\Delta L/\lambda$, where λ is the center laser wavelength of the comb) and a spectral resolution of $\Gamma_v = 6.6\,GHz$ (calculated as $\Gamma_v = c/(2F|\Delta L|)$, where c is the speed of light, and F is the cavity finesse), sufficient to detect absorption lines at atmospheric pressure in the flame, which have linewidths of $\sim 2\,GHz$ (half width at half maximum). After setting the desired VO, the scans of the PZT and the grating are synchronized to minimize the fluctuation of the open-loop error signal from the QD. Both PI controllers for active stabilization are then turned on to lock both scans.

Before the flame is switched on, a background spectrum is acquired by recording the Vernier spectrum of ambient air. After igniting the flame, the alignment of the cavity and the coupling efficiency to the PMF that guides the transmitted light are optimized. The PMF not only decouples the cavity alignment from the rest of the system, but also spatially filters out the higher order transverse modes transmitted through the cavity. For the acquisition of spectra, the CH_4 flow rate is fixed at 950 mL/min while the air flow rate is set to obtain the desired fuel-air equivalence ratio. The equivalence ratio is modulated by applying a square wave with a chosen frequency and duty cycle to the solenoid valve that controls the additional air supply. The HAB is set by tuning the vertical translation stage, where HAB = 0 was determined as the position where half of the transmitted power is cut by the burner.

2.4. Frequency calibration

The frequency axis of the acquired spectrum is calibrated using the etalon signal from PD 2. To obtain the pure etalon response, the background offsets of PD 2 and PD 1 are first subtracted from the etalon signal and the Vernier signal, respectively, and both signals are normalized to the same power level. The etalon signal is then divided by the Vernier signal to remove the power envelope and absorption features. The etalon fringes are finally obtained by band-pass filtering the signal to remove high-frequency noise and the remaining power envelope.

The consecutive zero crossings of the etalon fringes, whose spacing corresponds to half of the FSR ($\sim 27\,GHz$) of the CaF_2 window, are used as frequency markers. The frequency scale is obtained by linearly interpolating between these markers with a constant number of sampling points chosen so as to keep the total number of points in the spectrum unchanged, which yields a sample point spacing of $\sim 2\,GHz$. Next, the Vernier spectrum is linearly interpolated at these frequency coordinates. A normalized Vernier spectrum is obtained by dividing the calibrated Vernier spectrum by a background spectrum calibrated through the same procedure. Finally, the absolute frequency scale is retrieved by comparing the position of absorption lines in the normalized spectrum with a simulated spectrum of the target molecules.

2.5. Absorption sensitivity

The sensitivity was estimated by calculating the noise (σ) in the baseline as the standard deviation of the ratio between two consecutive background spectra, which was found to be equal to 2.3×10^{-3}. This corresponds to a noise equivalent absorption sensitivity of $4.0 \times 10^{-7}\,cm^{-1}$ $Hz^{-1/2}$, calculated as NEA = $\sigma T^{1/2}/L_{eff}$, in which T is the acquisition time of one scan (25 ms)

and $L_{eff} = 9.1$ m is the effective path length (FL/π) considering the 3.8 cm flame diameter and a finesse of 750. The NEA per spectral element, calculated as $NEA/M^{1/2}$ is 2.6×10^{-8} cm^{-1}Hz$^{-1/2}$, where M = 240 is the number of resolved elements ($\Gamma_V = 6.6$ GHz) in the spectral range used for the fit (1.6 THz).

3. Measurements in the flame

3.1. *H_2O and OH concentration retrieval at constant equivalence ratio*

Prior to investigating time-dependent processes in the flame, measurements at a constant fuel-air equivalence ratio $\phi = 1.00$ and different HABs were realized to evaluate the overall precision, sensitivity and accuracy of the instrument in concentration retrieval from a spectrum acquired in a single scan, as well as from a measurement series of several seconds. Simulations of the H_2O and OH concentrations as a function of HAB were carried out using Cantera [34] considering a one-dimensional burner-stabilized premixed flame model to obtain a reference for evaluation of accuracy.

For the concentration retrieval of H_2O and OH, we choose a spectral range spanning 13 nm around 1570 nm that contains several strong OH lines. In Fig. 2(a), a normalized spectrum from a single scan taken at HAB = 3.0 mm and $\phi = 1.00$ is presented (black markers) and compared to a fit of a Vernier spectrum model [30,31] considering both H_2O and OH absorption features (green curve). The residual of the fit is presented in Fig. 2(b). Most of the absorption features belong to H_2O, and a Vernier spectrum model considering only OH radical transitions is plotted in red to indicate the line positions for this species. The H_2O line parameters used in the model are taken from an experimental line list obtained from a spectrum measured in the same flame using comb-based Fourier transform spectroscopy under similar experimental conditions and HAB = 2.5 mm [36]. The Lorentzian half width of all H_2O absorption lines is set to 0.810 GHz, and the Doppler half-width to 0.713 GHz. The OH line list is taken from the HITRAN 2016 database [37], with the Lorentzian half width set to 2.04 GHz, according to an estimation from a previous work [38] using the same flame, and the Doppler half-width to 0.732 GHz. The VO number is set to −40, the flame diameter to 3.8 cm, and the flame temperature to 1950 K, the value determined from WMS measurements at HAB = 3.0 mm [35]. The normalized spectrum was multiplied by a constant factor to compensate for power variations between the background and flame spectra. The concentrations of H_2O and OH are retrieved from the fit to the entire spectral range shown in Fig. 2(a). The small number of OH lines compared to the continuum of H_2O absorption leads to a low weight of OH concentration in the computation of the goodness of the fit, and therefore the fit is repeated using only OH concentration as a fitting parameter in a narrower spectral range between 1572.0 and 1573.6 nm containing the 4 strongest OH lines [highlighted in blue in Fig. 2(a)], and using the H_2O concentration retrieved in the previous fit as a constant. Figures 2(c) and 2(e) show zooms of the two OH doublets used for concentration retrieval in the second step of the fit, along with their respective residuals in Figs. 2(d) and 2(f).

An overall good agreement between the model and the experimental spectrum is seen in Fig. 2, although a remaining structure in the residual is observed. An incomplete cancellation of absorption features in the etalon spectrum may introduce errors in the frequency calibration, but the level of residual that is typically observed in this case is considerably lower [32]. The structured residuum observed in the flame spectrum is caused mainly by missing transitions in the H_2O line list, particularly at wavelengths close to the OH transitions, since the line list does not contain lines that are within 0.02 cm^{-1} from an OH transition [36].

The retrieved concentrations of H_2O and OH are 17.3(4)% and 0.40(3)%, where the uncertainties are a combination of the precision at 25 ms obtained from the Allan variance analysis and the error in VO determination (described in detail in the next paragraphs). Other factors influencing the accuracy of concentration determination are the uncertainty of the water line intensities (up to 6% for the strongest lines and larger for weaker lines), and uncertainty of the flame temperature.
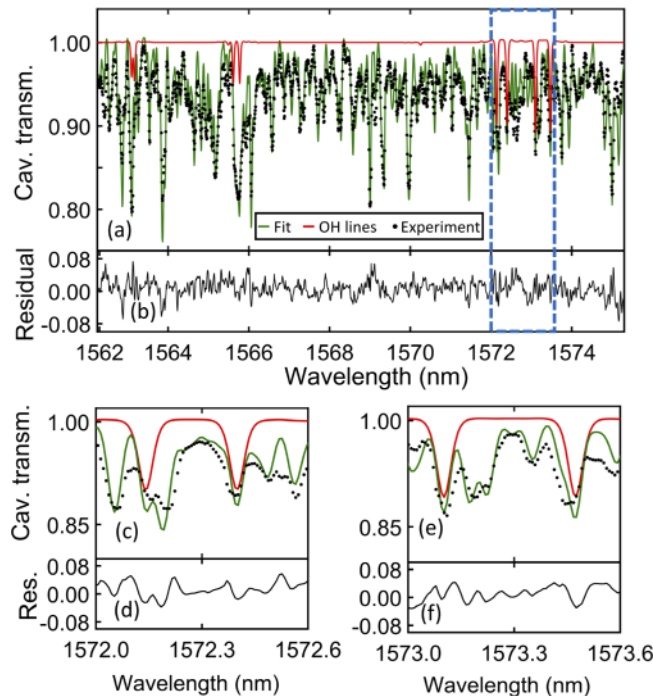
Fig. 2. (a) Single scan flame spectrum (black markers) measured at HAB = 3.0 mm, $\phi = 1.00$ and total flow of 10 L/min compared to a fit of a Vernier spectrum model considering both H_2O and OH transitions (green curve), and only OH (red curve). The spectral region used for retrieving the OH concentration is highlighted in blue. (b) Residual of the fit shown in (a). (c, e): Zooms of regions containing the strongest OH lines used to retrieve OH concentrations, along with the corresponding residuals (d, f).

The ± 50 K uncertainty, determined from WMS measurements [35], translates to a 2.5% relative uncertainty on the density of both species, as well as up to 3% uncertainty on the OH line intensities [37]. The H_2O and OH concentrations expected from Cantera simulations are 18.2% and 0.25%, respectively. A good agreement is observed for H_2O concentration, while the fitted OH concentration is largely overestimated. This deviation is not surprising: since H_2O lines close to OH lines are not included in the experimental line list [36], the fit attempts to compensate these missing H_2O lines by increasing the OH concentration. For example, in Fig. 2(e), a broader absorption feature at 1573.5 nm, where one of the strong OH lines is located, indicates the possible presence of additional H_2O lines not included in the model. It should be noted that Cantera simulations of OH concentrations have not previously been verified experimentally. One possible source of discrepancy are reactions at the flame boundary. However, these should be reduced to minimum by the nitrogen co-flow surrounding the flame.

The precision in concentration retrieval was estimated from the Allan-Werle analysis of H_2O and OH concentrations from a series of 4000 spectra (100 s) at HAB = 3.0 mm. In Fig. 3, the Allan variance for each analyte is shown (H_2O – blue open circles, OH – red diamonds). The white noise regime, represented by the black dashed lines, dominates up to 20 s. The standard deviations of H_2O and OH concentrations at 25 ms are 0.3% and 0.02%, respectively, which corresponds to relative precisions of 2% and 5% for H_2O and OH concentration in a single spectrum, respectively. Best precisions of 120 ppm for H_2O and 8 ppm for OH are obtained after 20 s of averaging.
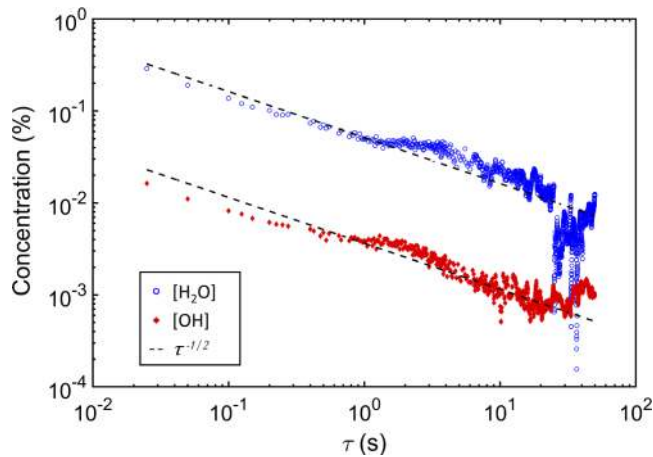
Fig. 3. Allan-Werle plots for H_2O (blue open circles) and OH (red diamonds) concentrations retrieved from fits, along with the curves corresponding to the white noise regime ($\tau^{-1/2}$ dependence, black dashed lines).

Another factor influencing the accuracy in concentration retrieval is the uncertainty in the VO determination. Experimentally, the VO is set by adjusting the translation stage on which one of the cavity mirrors is mounted. Therefore, the precision in setting the VO is limited by the micrometer screw resolution of ~5 µm, which corresponds to ~6 VOs. The exact VO cannot be retrieved from the fit: attempts to add the VO as another fitting parameter for the same series of spectra yielded VOs varying by about 10 units, which is unreasonable because the VO does not change during the measurement series (while the system is locked). To estimate how the VO determination affects the uncertainty in concentration retrieval, the Vernier spectrum model was fitted to the entire series of spectra with 7 different fixed VO values between −37 to −43. The results reveal changes in H_2O and OH concentrations of 0.05% and 0.003% per VO, respectively. The maximum uncertainty caused by the uncertainty in the VO determination is therefore 0.3% for H_2O and 0.02% for OH.

To further evaluate the accuracy and precision of our spectrometer, series of 400 spectra (10 s) were acquired at HABs ranging between 1.0 and 14.0 mm, and the concentrations were retrieved using the same procedure as described in the first paragraph of this section. Figure 4 shows the concentrations of both analytes ([H_2O] – blue open circles; [OH] – red diamonds) retrieved from each spectrum and averaged over the entire measurement series, along with the profiles simulated using Cantera for each species ([H_2O] – blue curve; [OH] – red curve). The error bars correspond to the precision at 25 ms obtained from the Allan-Werle analysis at each HAB. In this range of HABs the temperature of the flame varies in the interval 1900 - 1950 K [36], thus setting the temperature to 1950 K in all fits introduces a relative error in gas density and OH line strength of up to 3%, as described above.

The retrieved H_2O concentrations are in agreement with the Cantera simulation at lower HABs, but they deviate from the expected values as the HAB increases. This behavior has been observed before with WMS [35] and is caused by the decreasing flame diameter at higher HABs due to the cone-shaped flame. The retrieved OH concentrations are systematically overestimated at all HABs, which we believe can be explained by the missing transitions in the H_2O line list, as discussed previously for HAB = 3.0 mm.

The precision in H_2O concentration retrieval decreases with HAB, as seen in Fig. 4. The growing turbulence in the flame with increasing HAB disturbs the beam propagation through the flame, introducing fluctuations in the beam pointing during the scan. These disturbances
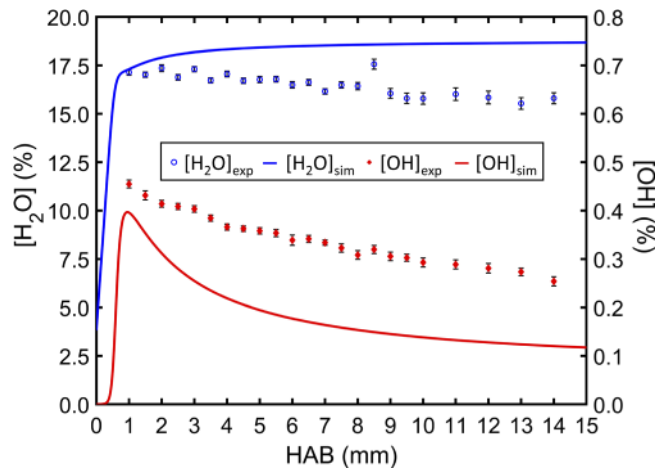
Fig. 4. Average H_2O (blue open circles) and OH (red diamonds) concentrations retrieved from fits to a 10 s series of flame spectra and one-dimensional Cantera simulations of the concentration profiles of H_2O (blue curve) and OH (red curve) as a function of HAB at $\phi = 1.00$. Error bars indicate the precision at 25 ms retrieved from the Allan-Werle analysis.

translate into power fluctuations of the transmitted beam and thus distortions in the laser power envelope, which affect the precision of the concentrations retrieved from the fit. Nevertheless, the precision at 25 ms remains at the few percent level, reaching a relative maximum of 4% at HAB = 12.0 mm. It is also worth mentioning that the spectrometer remains locked to a single VO during measurements up to HAB = 14.0 mm while the HAB is continuously changed by manual adjustments of the translation stage, indicating the robustness of the lock with respect to turbulences in the flame. The precision in OH concentration is less affected by changes in HAB. Since the OH concentrations are retrieved using a narrower range of the spectrum, the fit used for their retrieval is less sensitive to laser power envelope distortions.

Overall, fits to spectra measured in 25 ms with a constant ϕ yield high precision in concentration retrieval, which indicates the potential of the CF-VS spectrometer to monitor processes occurring in tens of milliseconds timescale, which is discussed in the next section.

3.2. Measurements with modulation of the equivalence ratio

Measurements with modulated fuel-air equivalence ratio – to introduce a periodic change of analyte concentrations in the flame – were performed at a fixed HAB of 3.0 mm. The equivalence ratio of the fuel was modulated between 0.87 and 1.00 with a square wave at frequencies ranging from 200 to 1800 mHz. The same fitting procedure as previously described was used for concentration retrieval. The temperature was again set to a constant value of 1950 K for the entire series of spectra.

Figures 5(a)–5(c) show the temporal profiles of H_2O (blue curves) and OH (red curves) concentrations retrieved from measurements at three different modulation frequencies, along with the modulation signal sent to the solenoid valve (gray curves). At 200 mHz, two flat regions in both concentration profiles are clearly distinguishable that correspond to the two steady-state equivalence ratios, with the transitions between them lasting hundreds of milliseconds. Such long-lasting transitions lead to the merging of adjacent cycles as the modulation frequency increases, setting an upper limit on modulation frequency to around 1800 mHz, above which no change in concentration can be observed because of the slow flame response. To determine the flame response time, modulations at a constant frequency of 1 Hz and duty cycles of the square wave ranging from 30 to 15% were carried out (pulse durations between 300 and 150 ms), and

the results are shown in Figs. 5(d)–5(f). From these temporal profiles, it is clear that changes in H_2O and OH concentrations can be detected at timescales down to 200 ms for OH, and 150 ms for H_2O. The overshoots, visible e.g. in Fig. 5(a), are caused by short instability in the air flow rate when the third mass flow controller (MFC 3) is switched on and off.
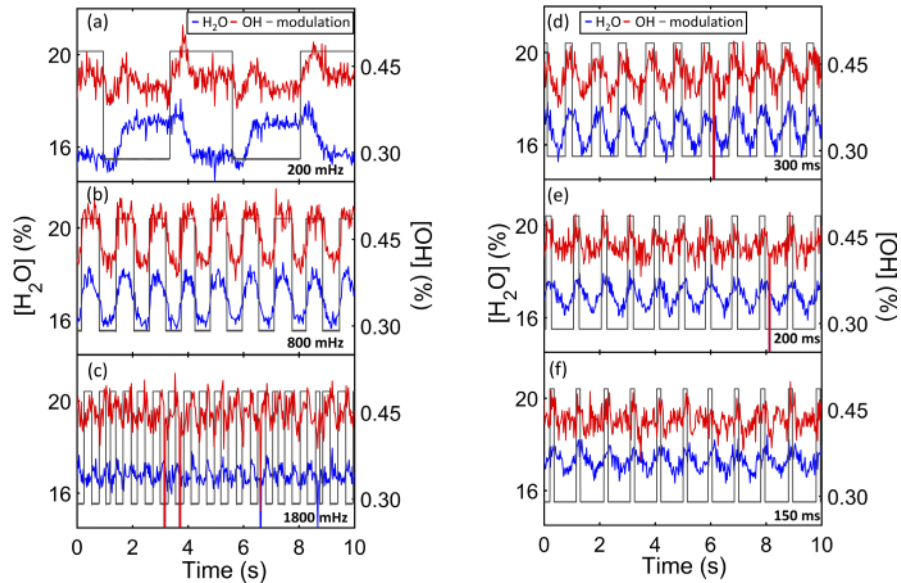

Fig. 5. H_2O (blue) and OH (red) concentrations retrieved from fits to spectra acquired at HAB = 3.0 mm while modulating ϕ between 0.87 and 1.00 with a square wave at different frequencies and duty cycles. Temporal profiles obtained with (a-c) 50% duty cycle square waves at the frequencies specified in the panels, and with (d-f) 1 Hz modulation and duty cycles ranging from 30 to 15%, corresponding to the pulse durations specified in the panels. The modulation signals are shown by the gray curves with arbitrary Y axes in all the panels.

To evaluate the stability of the concentration profiles over time, as well as to verify the agreement of the retrieved concentrations with the Cantera simulations, longer series of measurements (100 s) were carried out using a square wave modulation with 50% duty cycle at 200 mHz. One series was realized at HAB = 1.5 mm while modulating ϕ between 0.92 and 1.07, and the second was carried out at the same HAB and equivalence ratios as used for the series shown in Fig. 5(a). This particular choice of HABs and equivalence ratios was made to evaluate two distinct scenarios predicted by Cantera: the first is expected to yield significant changes in concentrations of both species with opposite phase, whereas the second should generate temporal profiles with similar variations in H_2O concentration but minor changes for OH.

Figures 6(a) and 6(b) show the measured concentration profiles at HAB = 1.5 and 3.0 mm, respectively. The red and blue curves show the H_2O and OH radical concentrations, respectively, with the 4000 modulation cycles overlapped, and the average of all cycles is shown in black. Figures 6(c) and 6(d) show the expected concentrations of both analytes obtained from Cantera simulations carried out for a range of equivalence ratios at the corresponding HABs. The values corresponding to the equivalence ratios used in the experiment are indicated by vertical green lines, and the experimental concentration values are marked by red and blue crosses. A comparison of the experimental steady-state concentrations with Cantera simulations reveals that the overall behavior agrees well with what is expected for each HAB and pair of ϕs. Although the absolute concentration values do not agree, the concentration ratios between the two steady-state regions are in good agreement with simulations for both analytes. These concentration ratios are

summarized in Table 1 for both measurement series, where the uncertainties are based on the standard deviation of all concentration values contained in each steady-state region, compared to ratios predicted from Cantera simulations. The agreement between the concentration ratios is better at HAB = 1.5 mm than at 3.0 mm. One possible explanation for this is that the change of the flame diameter with HAB is different for different ϕs, due to the change in total flow rate. Moreover, Cantera simulations predict temperature changes for the considered ϕs by about 17 K and 30 K at HABs of 1.5 and 3.0 mm, respectively. Thus setting the temperature to 1950 K in the model introduces a larger error at HAB = 3.0 mm than at 1.5 mm.
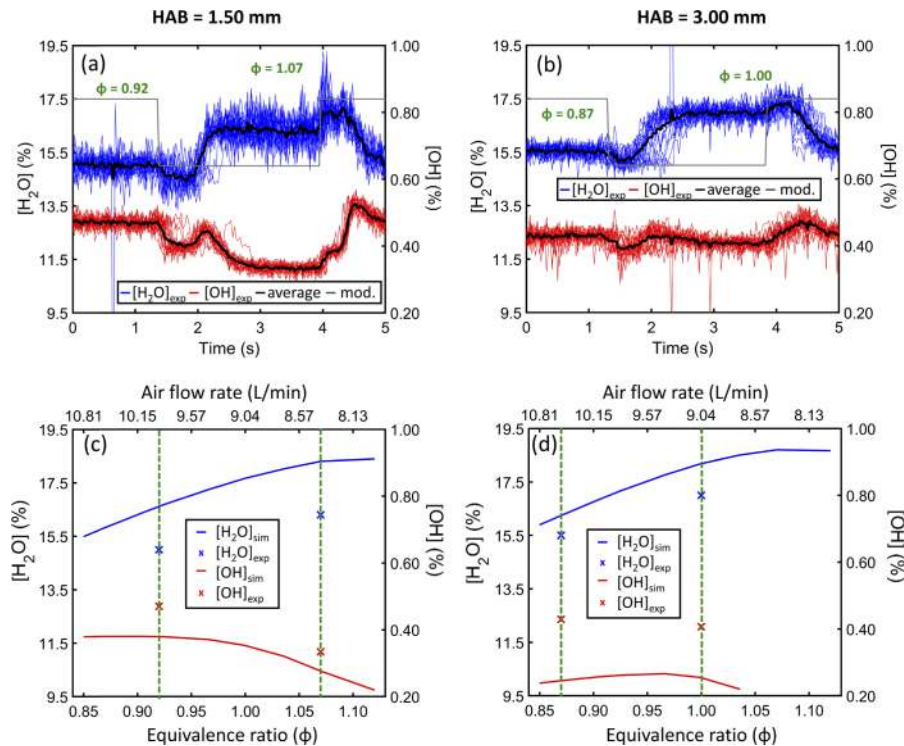

Fig. 6. (a, b): Experimental temporal profiles of H_2O (blue) and OH (red) concentrations retrieved from a 100 s series of measurements taken while modulating the equivalence ratio at 200 mHz, with every cycle overlapped and plotted along with the average of all cycles (black). The modulation signals are shown by the gray curves with arbitrary Y axes in both panels. (c, d): One-dimensional Cantera simulations of H_2O (blue) and OH (red) concentrations at different equivalence ratios and CH_4 flow rate set to 950 mL/min. The equivalence ratios corresponding to the high/low levels of the modulation in (a) and (b) are marked by vertical green dashed lines, and the mean value of the experimentally obtained steady-state concentrations are indicated by solid markers. Measurements and simulations shown in the left (a, c) and right (b, d) plots were carried out at HAB = 1.5 and 3.0 mm, respectively.

The overlapped temporal profiles reveal that the transient features between the steady-state conditions for every cycle of modulation are repeatable over the entire measurement series and clearly resolved. However, interpretation of H_2O and OH concentrations in those regions is not possible with one-dimensional Cantera simulations, since they assume constant equivalence ratios and cannot predict intermediate states. Moreover, the flame becomes visibly inhomogeneous during the times at which the additional air flow is switched on or off, and therefore the part of the flame that is probed by the beam can no longer be regarded as representative for the whole

Table 1. Experimental and simulated H_2O and OH concentration ratios for each pair of ϕs.

HAB (mm)	Concentration ratios	Fit	Cantera simulation
1.5	$[H_2O]_{\phi=1.07}/[H_2O]_{\phi=0.92}$	1.09(1)	1.10
	$[OH]_{\phi=1.07}/[OH]_{\phi=0.92}$	0.71(3)	0.73
3.0	$[H_2O]_{\phi=1.00}/[H_2O]_{\phi=0.87}$	1.092(5)	1.120
	$[OH]_{\phi=1.00}/[OH]_{\phi=0.87}$	0.95(2)	1.04

plane at a given HAB. Nevertheless, the consistency of such features reveals that CF-VS can be employed to extract quantitative information from these transient regions.

4. Conclusions and outlook

We demonstrated for the first time cavity-enhanced comb-based spectroscopy in a flame with 25 ms time resolution and percent level precision in concentration determination of two typical combustion analytes. The CF-VS spectrometer is able to track changes in concentrations of both H_2O and OH radical while the fuel/air equivalence ratio is modulated, yielding temporal profiles consistent with the applied modulation and revealing repeatable transient features between the two steady states. A good agreement between the retrieved steady-state H_2O concentrations and the one-dimensional Cantera simulations was achieved, while the OH concentrations were overestimated due to missing transitions of the continuum of H_2O absorption in the line list used for modelling the Vernier spectrum. The high precision in concentration retrieval at 25 ms was maintained in measurements with different degrees of instability – introduced by changing the HAB – revealing the robustness of the spectrometer. The CF-VS spectrometer can be implemented also in the mid-infrared region – as previously demonstrated for static measurements [31,32] – where a wider range of chemical species can be detected with even higher sensitivity. Thus CF-VS is promising not only for combustion diagnostics but also for other gas sensing applications that require in situ multispecies quantification in timescales of tens of milliseconds, such as atmospheric monitoring.

References

1. N. Docquier and S. Candel, "Combustion control and sensors: a review," Prog. Energy Combust. Sci. **28**(2), 107–150 (2002).
2. K. Kohse-Höinghaus, R. S. Barlow, M. Aldén, and J. Wolfrum, "Combustion at the focus: laser diagnostics and control," Proc. Combust. Inst. **30**(1), 89–123 (2005).
3. M. Aldén, J. Bood, Z. Li, and M. Richter, "Visualization and understanding of combustion processes using spatially and temporally resolved laser diagnostic techniques," Proc. Combust. Inst. **33**(1), 69–97 (2011).
4. A. Ehn, J. Zhu, X. Li, and J. Kiefer, "Advanced laser-based techniques for gas-phase diagnostics in combustion and aerospace engineering," Appl. Spectrosc. **71**(3), 341–366 (2017).
5. C. Schulz and V. Sick, "Tracer-LIF diagnostics: quantitative measurement of fuel concentration, temperature and fuel/air ratio in practical combustion systems," Prog. Energy Combust. Sci. **31**(1), 75–121 (2005).
6. S. Roy, J. R. Gord, and A. K. Patnaik, "Recent advances in coherent anti-Stokes Raman scattering spectroscopy: Fundamental developments and applications in reacting flows," Prog. Energy Combust. Sci. **36**(2), 280–306 (2010).
7. J. Kiefer and P. Ewart, "Laser diagnostics and minor species detection in combustion using resonant four-wave mixing," Prog. Energy Combust. Sci. **37**(5), 525–564 (2011).

8. H. A. Michelsen, C. Schulz, G. J. Smallwood, and S. Will, "Laser-induced incandescence: Particulate diagnostics for combustion, atmospheric, and industrial applications," Prog. Energy Combust. Sci. **51**, 2–48 (2015).
9. R. K. Hanson, "Applications of quantitative laser sensors to kinetics, propulsion and practical energy systems," Proc. Combust. Inst. **33**(1), 1–40 (2011).
10. C. S. Goldenstein, R. M. Spearrin, J. B. Jeffries, and R. K. Hanson, "Infrared laser-absorption sensing for combustion gases," Prog. Energy Combust. Sci. **60**, 132–176 (2017).
11. J. A. Silver and D. J. Kane, "Diode laser measurements of concentration and temperature in microgravity combustion," Meas. Sci. Technol. **10**(10), 845–852 (1999).
12. X. Chao, J. B. Jeffries, and R. K. Hanson, "Wavelength-modulation-spectroscopy for real-time, in situ NO detection in combustion gases with a 5.2 μm quantum-cascade laser," Appl. Phys. B: Lasers Opt. **106**(4), 987–997 (2012).
13. S. Cheskis, I. Derzy, V. A. Lozovsky, A. Kachanov, and D. Romanini, "Cavity ring-down spectroscopy of OH radicals in low pressure flame," Appl. Phys. B: Lasers Opt. **66**(3), 377–381 (1998).
14. I. Derzy, V. A. Lozovsky, and S. Cheskis, "Absolute CH concentration in flames measured by cavity ring-down spectroscopy," Chem. Phys. Lett. **306**(5-6), 319–324 (1999).
15. B. P. Wilcox, E. T. H. Chrysostom, A. McIlroy, J. W. Daily, and I. M. Kennedy, "Measurement of CrO in flames by cavity ringdown spectroscopy," Appl. Phys. B: Lasers Opt. **77**(5), 535–540 (2003).
16. A. Schocker, K. Kohse-Höinghaus, and A. Brockhinke, "Quantitative determination of combustion intermediates with cavity ring-down spectroscopy: systematic study in propene flames near the soot-formation limit," Appl. Opt. **44**(31), 6660–6672 (2005).
17. M. Lackner, "Tunable diode laser absorption spectroscopy (TDLAS) in the process industries - a review," Rev. Chem. Eng. **23**(2), 65–147 (2007).
18. C. Liu and L. Xu, "Laser absorption spectroscopy for combustion diagnosis in reactive flows: A review," Appl. Spectrosc. Rev. **54**(1), 1–44 (2019).
19. C. Abd Alrahman, A. Khodabakhsh, F. M. Schmidt, Z. Qu, and A. Foltynowicz, "Cavity-enhanced optical frequency comb spectroscopy of high-temperature H_2O in a flame," Opt. Express **22**(11), 13889–13895 (2014).
20. P. J. Schroeder, R. J. Wright, S. Coburn, B. Sodergren, K. C. Cossel, S. Droste, G. W. Truong, E. Baumann, F. R. Giorgetta, I. Coddington, N. R. Newbury, and G. B. Rieker, "Dual frequency comb laser absorption spectroscopy in a 16 MW gas turbine exhaust," Proc. Combust. Inst. **36**(3), 4565–4573 (2017).
21. A. D. Draper, R. K. Cole, A. S. Makowiecki, J. Mohr, A. Zdanowicz, A. Marchese, N. Hoghooghi, and G. B. Rieker, "Broadband dual-frequency comb spectroscopy in a rapid compression machine," Opt. Express **27**(8), 10814–10825 (2019).
22. R. S. Watt, T. Laurila, C. F. Kaminski, and J. Hult, "Cavity enhanced spectroscopy of high-temperature H_2O in the near-infrared using a supercontinuum light source," Appl. Spectrosc. **63**(12), 1389–1395 (2009).
23. T. Werblinski, F. Mittmann, M. Altenhoff, T. Seeger, L. Zigan, and S. Will, "Temperature and water mole fraction measurements by time-domain-based supercontinuum absorption spectroscopy in a flame," Appl. Phys. B: Lasers Opt. **118**(1), 153–158 (2015).
24. L. A. Kranendonk, X. An, A. W. Caswell, R. E. Herold, S. T. Sanders, R. Huber, J. G. Fujimoto, Y. Okura, and Y. Urata, "High speed engine gas thermometry by Fourier-domain mode-locked laser absorption spectroscopy," Opt. Express **15**(23), 15115–15128 (2007).
25. T. Werblinski, P. Fendt, L. Zigan, and S. Will, "High-speed combustion diagnostics in a rapid compression machine by broadband supercontinuum absorption spectroscopy," Appl. Opt. **56**(15), 4443–4453 (2017).
26. D. S. Dandy and S. R. Vosen, "Numerical and experimental studies of hydroxyl radical chemiluminescence in methane-air fames," Combust. Sci. Technol. **82**(1-6), 131–150 (1992).
27. A. Choudhuri, "Intermediate radical concentrations in hydrogen–natural gas blended fuel jet flames," Int. J. Hydrogen Energy **29**(12), 1293–1302 (2004).
28. M. Zhao, D. Buttsworth, and R. Choudhury, "Experimental and numerical study of OH* chemiluminescence in hydrogen diffusion flames," Combust. Flame **197**, 369–377 (2018).
29. L. Rutkowski and J. Morville, "Broadband cavity-enhanced molecular spectra from Vernier filtering of a complete frequency comb," Opt. Lett. **39**(23), 6664–6667 (2014).
30. L. Rutkowski and J. Morville, "Continuous Vernier filtering of an optical frequency comb for broadband cavity-enhanced molecular spectroscopy," J. Quant. Spectrosc. Radiat. Transfer **187**, 204–214 (2017).
31. A. Khodabakhsh, V. Ramaiah-Badarla, L. Rutkowski, A. C. Johansson, K. F. Lee, J. Jiang, C. Mohr, M. E. Fermann, and A. Foltynowicz, "Fourier transform and Vernier spectroscopy using an optical frequency comb at 3–5.4 μm," Opt. Lett. **41**(11), 2541–2544 (2016).
32. A. Khodabakhsh, L. Rutkowski, J. Morville, and A. Foltynowicz, "Mid-infrared continuous-filtering Vernier spectroscopy using a doubly resonant optical parametric oscillator," Appl. Phys. B: Lasers Opt. **123**(7), 210 (2017).
33. G. Hartung, J. Hult, and C. F. Kaminski, "A flat flame burner for the calibration of laser thermometry techniques," Meas. Sci. Technol. **17**(9), 2485–2493 (2006).
34. D. Goodwin, "Cantera: An object-oriented software toolkit for chemical kinetics, thermodynamics, and transport properties," Pasadena, CA (2016).
35. Z. Qu, R. Ghorbani, D. Valiev, and F. M. Schmidt, "Calibration-free scanned wavelength modulation spectroscopy – application to H_2O and temperature sensing in flames," Opt. Express **23**(12), 16492–16499 (2015).

36. L. Rutkowski, A. Foltynowicz, F. M. Schmidt, A. C. Johansson, A. Khodabakhsh, A. A. Kyuberis, N. F. Zobov, O. L. Polyansky, S. N. Yurchenko, and J. Tennyson, "An experimental water line list at 1950 K in the 6250–6670 cm^{-1}," J. Quant. Spectrosc. Radiat. Transfer **205**, 213–219 (2018).

37. I. E. Gordon, L. S. Rothman, C. Hill, R. V. Kochanov, Y. Tan, P. F. Bernath, M. Birk, V. Boudon, A. Campargue, K. V. Chance, B. J. Drouin, J.-M. Flaud, R. R. Gamache, J. T. Hodges, D. Jacquemart, V. I. Perevalov, A. Perrin, K. P. Shine, M.-A. H. Smith, J. Tennyson, G. C. Toon, H. Tran, V. G. Tyuterev, A. Barbe, A. G. Császár, V. M. Devi, T. Furtenbacher, J. J. Harrison, J.-M. Hartmann, A. Jolly, T. J. Johnson, T. Karman, I. Kleiner, A. A. Kyuberis, J. Loos, O. M. Lyulin, S. T. Massie, S. N. Mikhailenko, N. Moazzen-Ahmadi, H. S. P. Müller, O. V. Naumenko, A. V. Nikitin, O. L. Polyansky, M. Rey, M. Rotger, S. W. Sharpe, K. Sung, E. Starikova, S. A. Tashkun, J. Vander Auwera, G. Wagner, J. Wilzewski, P. Wcisło, S. Yu, and E. J. Zak, "The HITRAN2016 molecular spectroscopic database," J. Quant. Spectrosc. Radiat. Transfer **203**, 3–69 (2017).

38. L. Rutkowski, A. C. Johansson, D. Valiev, A. Khodabakhsh, A. Tkacz, F. M. Schmidt, and A. Foltynowicz, "Detection of OH in an atmospheric flame at 1.5 μm using optical frequency comb spectroscopy," Photonics Lett. Pol. **8**(4), 110–112 (2016).